Instrument Performance of the Ocean Color Imager

Li-Shing Lee[1] and Yi-Jye Chiang[1]

ABSTRACT

The Ocean Color Imager is an electro-optic remote sensing instrument with a 702 km swath width and 800 m resolution on board the ROCSAT-1 satellite that was launched in January 1999. It is the first push-broom type spectral-radiometer for measuring radiance from ocean surfaces and atmospheric scattering in six visible and near infrared bands for application research in ocean optics. Described in this paper are OCI's major characteristics, parameters and pre-launch and post-launch performance test results including SNR, MTF, image sharpness, band to band spectral registration and anti-blooming performance.

(Key words: Ocean Color Imager, ROCSAT-1, Remote sensing, Signal to noise ratio, Modulation transfer function, Image sharpness, Band to band spectral registration, Anti-blooming)

1. INTRODUCTION

The first satellite of the Republic of China on Taiwan, ROCSAT-1, was launched in January 1999. The Satellite has three scientific payload instruments including the Ocean Color Imager (Fig. 1), or OCI, which is a spectral radiometer as well as a nadir looking push-broom imager that can acquire data of radiance from the ocean surface and atmospheric scattering in six visible and near infrared bands for application research in ocean optics..

Since the late 1970's, space-borne ocean observation instruments, such as CZCS (1978-1986), OCTS (1996-1997), and SeaWiFS (1997-), have acquired many high quality images for accessing the ocean's role in the global carbon cycle, elucidating the magnitude and variability of the primary productivity by phytoplankton, and determining the distribution and timing of spring booms. By using rotating mirrors as the scanning mechanism, their major characteristics and parameters (Table 1) include, among others, a very wide field of view (FOV) for observing large areas and a very high signal to noise ratio (SNR) to provide reliable data for estimating water-leaving radiance from the ocean surface.

[1]National Space Program Office, No.9, 8th floor, Prosperity Road I, Science Based Industrial Park, Hsin-Chu, Taiwan, ROC
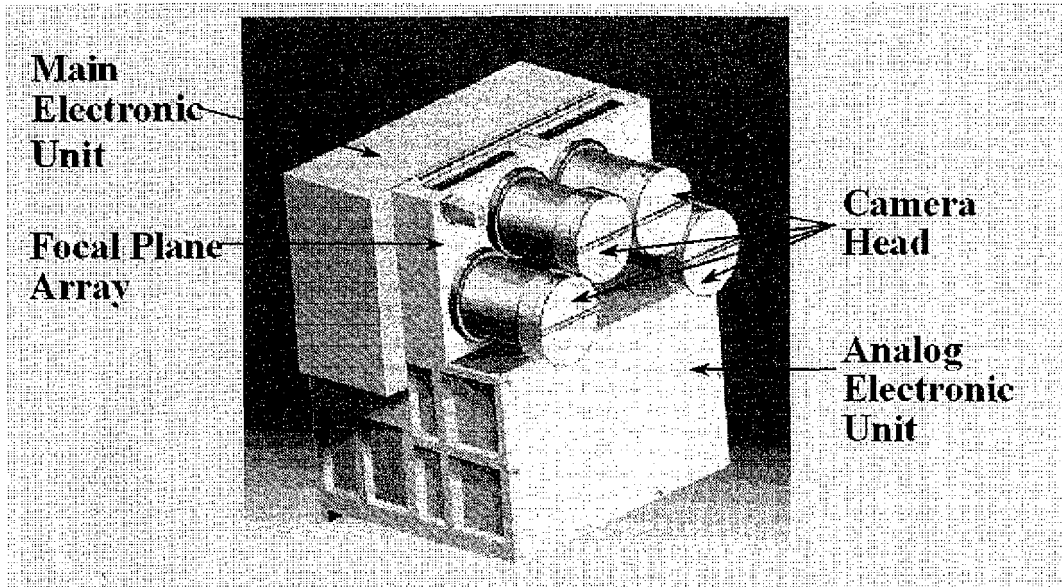
Fig. 1. Outlook of the OCI.

The push-broom scanning mechanism has been utilized to make remote sensing instruments on several land observing satellites, such as the SPOT series and IRS, of which major characteristics and parameters include very high ground resolution with relatively narrow FOV and low SNR. (Table 2) To simplify interface development and reduce risks in instrument engineering, no moving parts were used to make the three payload instruments on the ROCSAT-1. Consequently, instead of a rotating mirror, the OCI employed a push-bloom scanning mechanism, and achieving very high SNR, very wide FOV, and accurate radiometric calibration became tasks with unprecedented challenge in developing this kind of remote sensing instrument.

2. MISSIONS AND BAND SELECTION FOR SCIENTIFIC OBSERVATIONS

The ROCSAT-1 program, including the OCI, is managed by the National Space Program Office (NSPO) of the Republic of China. The ROCSAT-1 orbit is at an altitude of 600 km with a 35° inclination angle, and is not sun synchronous. This orbit was selected with the consideration of maximizing contact time with the ground station in Taiwan and fulfilling the necessity of another payload, Ionospheric Plasma Electrodynamics Instrument (IPEI), to gain more operation time near the equator. The OCI was originally planned to take images between 9:00 AM and 3:00 PM local time and the acquired data would be available to all interested scientists for doing research subjects in:

-mapping the pigment distribution in the low-latitude oceans and generating surface spectral data;

Table 1 Major Characteristics and Parameters of Ocean Observation Satellites

Satellite		NIMBUS	ADEOS	SEASTAR	ROCSAT-1
Sensor		CZCS	OCTS	SeaWiFS	OCI
Observation Target		Ocean	Ocean	Ocean	Ocean
Scanning Mechanism		Rotating Mirror	Rotating Mirror	Rotating Mirror	Push-Broom
Field of View		± 20°	± 40°	± 53°	± 30°
Band Selection	Vis	4 Bands	6 Bands	6 Bands	5 Bands
	NIR	1 Band	2 Bands	2 Bands	1 Band
	MWIR	0 Band	1 Bands		
	TIR	1 Band	3 Bands		
Signal to Noise Ratio (Vis Bands)		200-300	450-500	440-670	650-780
Orbit Type		Sun Sync. at 955 km	Sun Sync. at 797 km	Sun Sync. at 705 km	35° inclination. at 600 km
Ground Resolution		825 m	700 m	1100 m	800 m

Table 2 Major characteristics and parameters of some land observation satellites

Satellite		SPOT-1,2 & 3	SPOT-4	IRS-1
Observation Target		Land	Land	Land
Scanning Mechanism		Push-Broom	Push-Broom	Push-Broom
Field of View		± 2.75°	± 2.75°	± 4.7°
Band Selection	Vis	2 Bands	2 Bands	3 Bands
	NIR	1 Band	1 Band	1 Band
	SWIR		1 Band	
Signal to Noise Ratio		100 - 300	100 - 300	100 - 200
Orbit Type		Sun Sync. at 832 km	Sun Sync. at 832 km	Sun Sync. at 904 km
Ground Resolution		10-20 m	10-20 m	36.25 m

-studying marine productivity and the dynamics of meso-scale eddies; and

-investigating the influence of atmospheric aerosols in remote sensing.

Besides a redundant 555 nm band, the OCI has six different visible and near IR spectral bands (Table 3) that are similar to, but fewer than the SeaWiFS'. Since there is little water-leaving radiance from the ocean surface in the spectral regions near 670 nm and 869 nm, B5 and B6 are mainly for measuring atmospheric scattering with the measured data to be used for atmospheric correction. The data acquired from the other bands are from both atmospheric scattering and reflectance from the ocean surface. After correction, by subtracting the estimated radiance of atmospheric scattering, water leaving radiance values can be obtained and used to compute the pigment distribution near the ocean surface by using the validation and calibration algorithms developed by the science team.

3. SYSTEM ARCHITECTURE

The OCI's hardware was built by the NEC Corporation and consists of three modules: the Optical Unit (OU), the Analog Electronic Unit (AEU), and the Main Electronic Unit (MEU). Its functional block diagram is shown in Fig. 2.

The OU consists of four camera heads with seven focal planes each with a Thomson TH7811 linear array CCD device for detecting the input radiance. Each camera head has an eight-lens telecentric telescope subsystem (Fig. 3) with a 19.5 mm focal length and a 60.7° field of view (FOV) to give a 702 km swath width at an altitude of 600 km. Two focal planes (B1/B3, B2/B4, or B5/B6) share a camera head and B7 uses a stand-alone camera head with a lens subsystem similar to that of the others.

The TH7811 linear CCD device has 1728 cells each with a 13μ m $\times$ 13 μ m photosite that can transform optical radiance into electric current. The cells in each device are arranged to give 832 double cell pixels plus 64 single cell pixels in the center region of the array. At an altitude of 600 km and with a 19.5 mm focal length, 6.9 km/s ground track speed and 115.8 ms

Table 3. The OCI band selection and scientific observation

Band Number	Center Wavelength	Bandwidth, FWHM	Scientific Observation
B1	444 nm	20.0 nm	Chlorophyll Absorption
B2	492 nm	20.1 nm	Pigment
B3	512 nm	19.6 nm	Chlorophyll Absorption
B4	555 nm	18.5 nm	Hinge point, Sediments
B5	670 nm	18.5 nm	Atmospheric Scattering
B6	869 nm	40.3 nm	Atmospheric Scattering
B7	555 nm	18.5 nm	Hinge point, Sediments

Optical Unit **Electronics Unit** **Spacecraft BUS**
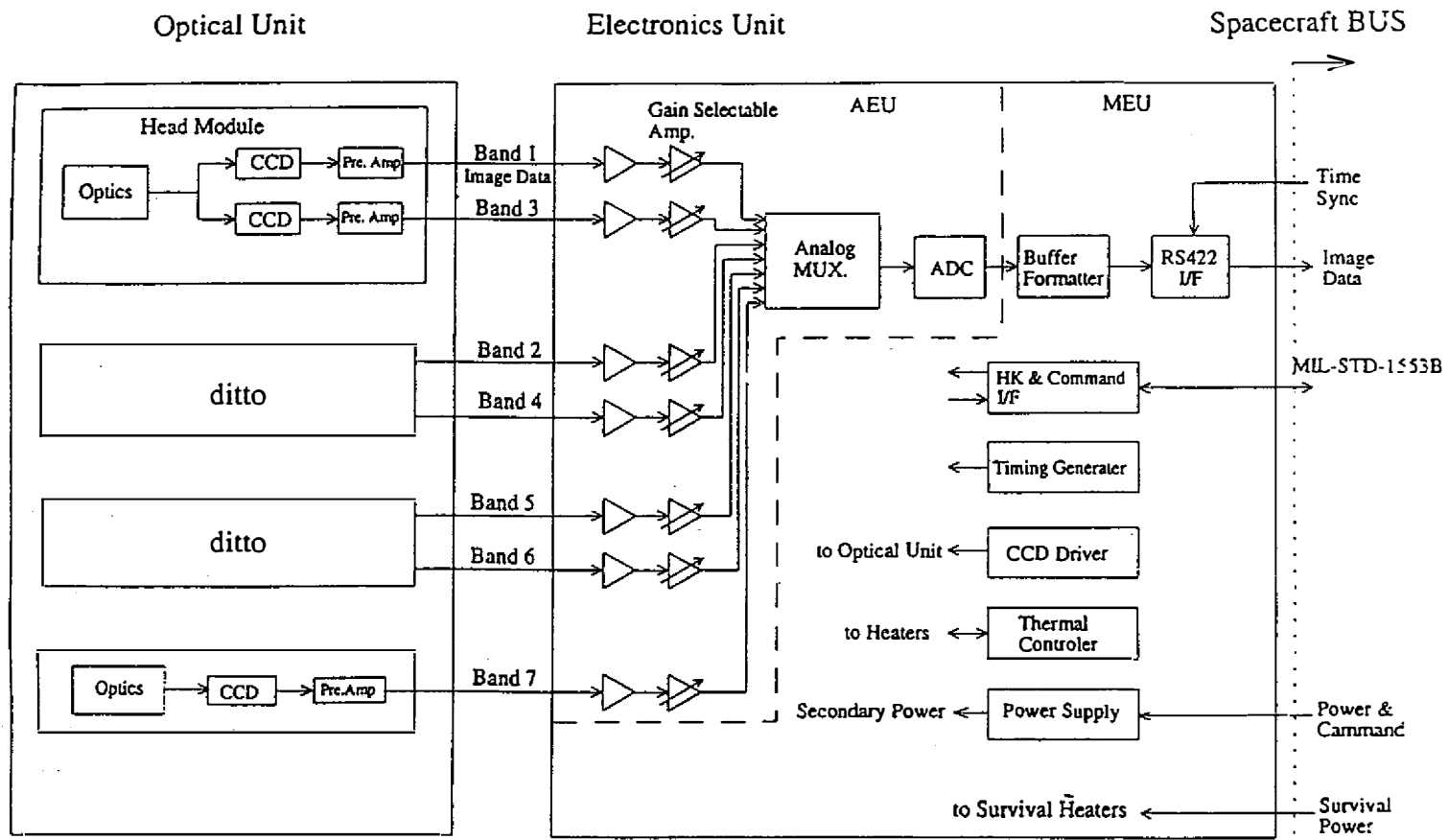
Fig.2. Functional block diagram of the OCI.
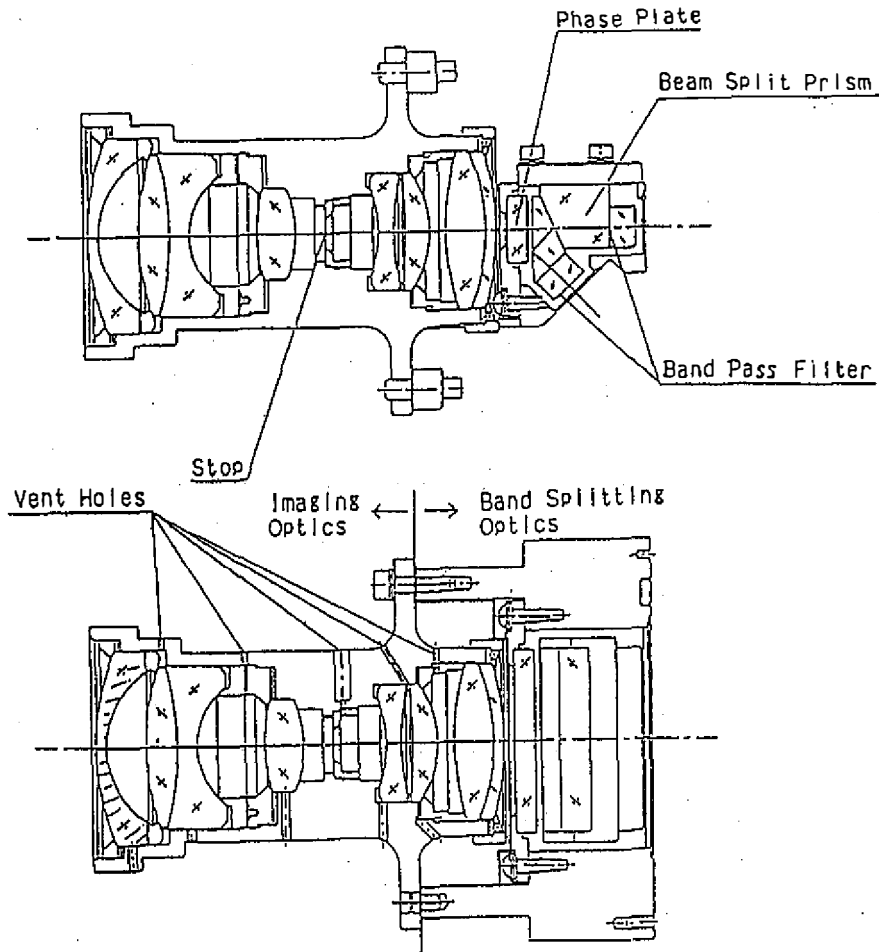
Fig.3. Side view and top view of a cut-away camera head.

integration time, the nadir-looking push-broom mechanism gives ~800m × 800 m ground resolution for the double cell pixel and ~400 m × 800 m ground resolution for the single cell pixel.

4. RESULTS OF PERFORMANCE TESTS

The results of selected pre-launch and post-launch performance tests are described in the following sections.

4.1 Signal To Noise Ratio

To assure good image quality, various techniques were developed to minimize noise in the signal chain and achieve very high SNR values (Table 4). These techniques included:
• widening the telescope aperture to enhance the input signal;

- keeping the CCD operation temperature at ~10°C to lower the thermal noise;
- using a clamp and sample circuit to perform correlated double sampling;
- good shielding to block electro-magnetic interference as much as possible; and
- digitizing the signal into 12 bits to make the quantization noise insignificant.

The pre-launch SNR was measured using a very stable integrating sphere as the light source and the results, given in Fig. 4, indicated that the SNR values would be at least 650 with mean input radiance and higher than 300 even with relatively weak input radiance, ~1/5 of the corresponding mean radiance. Such high performance suggested that the sensor's observation time could be expanded from 9:00-15:00 to 7:30-16:30 local time at least.

We also performed post-launch SNR measurements by analyzing radiance data from a selected region in an acquired image with (apparently) uniform total radiance. Its radiance value was measured to be ~ 0.45 times that of the mean value and was > 570 times the noise level. This SNR value was similar to, but slightly lower than, the pre-launch SNR value, ~ 600 at the same radiance. The difference could be attributed to non-uniformity of the radiance from the selected region. An example of comparison is shown in Fig. 5.

4.2 Radiometric Calibration and Image Quality

When the OCI is observing an oceanic region without cloud and sun-glint, its total input radiance can be expressed as follows

$$It = Ir + Ia + t \; lw \tag{1}$$

Table 4 . Specification of SNR and pre-launch performance test results.

Band No.	Specification		Pre-launch Performance Test Results	
	Mean Radiance*	SNR	Input Radiance*	SNR
B1	84.1	$\geq$450	84.1	$\geq$751
B2	65.6	$\geq$450	61.3	$\geq$779
B3	56.4	$\geq$450	54.1	$\geq$782
B4	45.7	$\geq$450	42.9	$\geq$657
B5	24.6	$\geq$350	24.15	$\geq$777
B6	10.9	$\geq$350	10.6	$\geq$671
B7	45.7	$\geq$450	42.9	$\geq$700

* Unit of W/(Sr-m^2-μ m)
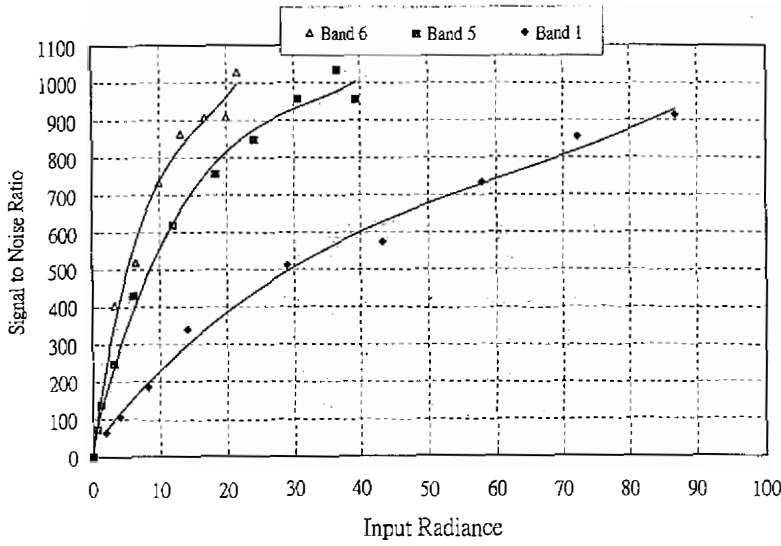
Fig.4. Examples of typical relation between SNR and input radiance. The data are from pixel #99, B6, B5, and Bl. The results indicate that SNR decreases as input radiance weakens. However, SNR remains high (>300) even with 1/5 of the mean radiance, i.e., 2.2, 4.9, and 17 W/(Sr-m²-μm) for B6, B5, and B l respectively.

OCI-Band 2-Pixel #584
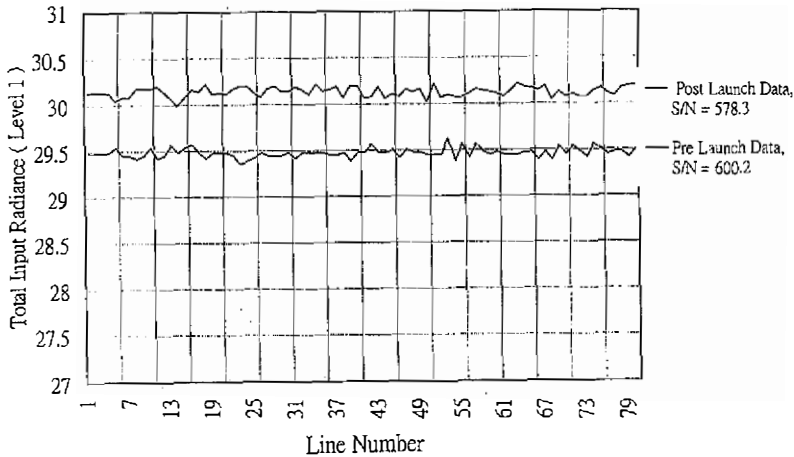
Fig. 5. An example of SNR comparison between pre-launch and post-launch data from pixel # 584 of band # 2. The output signals were sampled 80 times when the OCI was used to view steady and uniform light sources. The pre-launch data showed that the output signal was ~600 times greater than the standard deviation, or noise, and the post-launch data showed that SNR was ~578.

where I_r, I_a and I_w represent Rayleigh scattering, aerosol scattering and water-leaving radiance, respectively, and t is diffuse transmittance. The value of I_w is used to estimate the amount of pigment in the ocean and it is desirable to calculate this value by removing the atmospheric components, i.e., Rayleigh scattering and aerosol scattering, from the total input radiance.

Before launch the OCI was calibrated with a standard light source and the signal chain of the calibration process could be expressed as follows:

[Radiance from the Standard Light Source] → (The OCI) → [Digitized Output Signal]

where the light source was a well calibrated integrating sphere with 97% absolute accuracy and 99.5% uniformity. The calibration results provided useful parameters for computing total input radiance from the OCI's digitized data, as follows:

$$I_t = P + Q \cdot x + R \cdot x^2 + S \cdot x^3 \qquad (2)$$

where x was the OCI's digitized signal and P, Q , R, and S were calibration parameters that varied from band to band and from pixel to pixel. Unlike other space-borne ocean observation instruments, such as CZCS, OCTS, and SeaWiFS, that utilized rotating mirror architecture with only one photodetector to measure the input radiance for each spectral band, the OCI had 896 CCD pixels (detectors) to measure the input radiance for each spectral band. It took a great deal of effort to achieve so many values for P, Q, R, and S for the pixels by performing radiometric calibration.

Since I_w generally constitutes less than 20% of I_t, a small uncertainty in the calibration parameter due to·non-uniformity of the standard light source could have a big impact on computing I_w, and, moreover, degrade the image quality of the pigment distribution significantly because the relation between I_w and pigment concentration is largely logarithmical. Specifically, we have found that a 0.5% uncertainty due to non-uniformity of radiance from the standard light source would lead to a ~2.5% uncertainty in the computed I_w, and eventually a ~15% uncertainty in the computed concentration of pigments, such as chlorophyll-a. As a result the image quality would be degraded by non-periodic vertical stripes (Fig. 6) arising from uncertainty of the derived pigment concentration originated from inaccuracy of relative calibration among the CCD pixels due to non-uniformity of radiance from the standard light source.

This phenomenon, the presence of non-periodic vertical stripes originating from non-uniformity of radiance from the standard light source, has not been found in ocean color imagery from any other space-borne ocean observation instruments because, instead of several hundred CCD pixels, they have used only one photodetector for each spectral band. The phenomenon has not been seen in images provided by any space-borne land observation instruments, including those with a push-broom scanning mechanism such as SPOT and IRS, because the data processing for land imagery is much less sensitive to I_t uncertainty than that for ocean imagery.
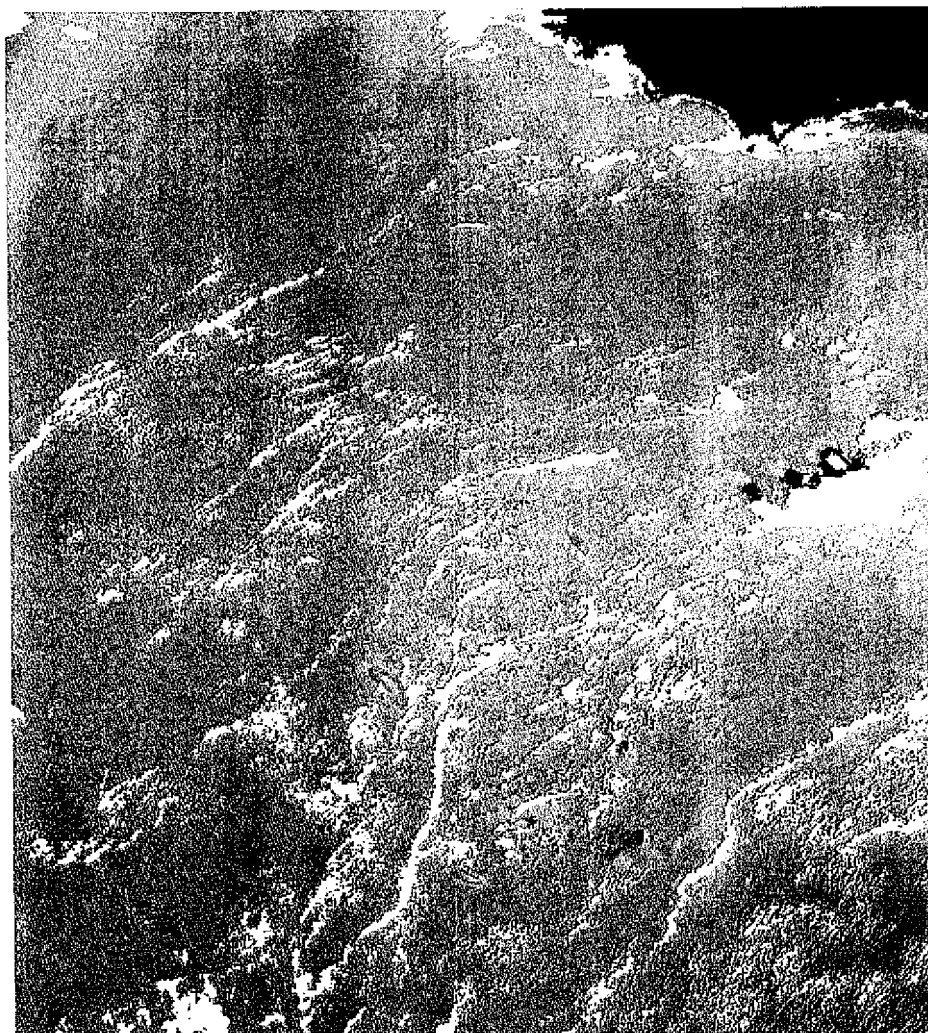
Fig.6. An OCI's image of chlorophyll-a distribution in South China Sea. The
quality is degraded by non-periodic vertical stripes arising from uncer-
tainty of the derived pigment concentration that originated from inaccu-
racy of relative calibration among the CCD pixels due to non-uniformity
of radiance from the standard light source.

It is therefore a task with unprecedented challenge to improve the OCI's image quality by
modifying the calibration parameters to eliminate the non-periodic vertical stripes. We have
very carefully analyzed many post-launch data taken by the OCI over regions with uniform
radiance (SNR $\geq$ 500) and used the results to modify the original calibration parameters. The
modified parameters, with less than 0.2% inaccuracy in relative calibration among the CCD
pixels, would lead to a ~1% uncertainty in I_w computation and a ~5% uncertainty in pigment
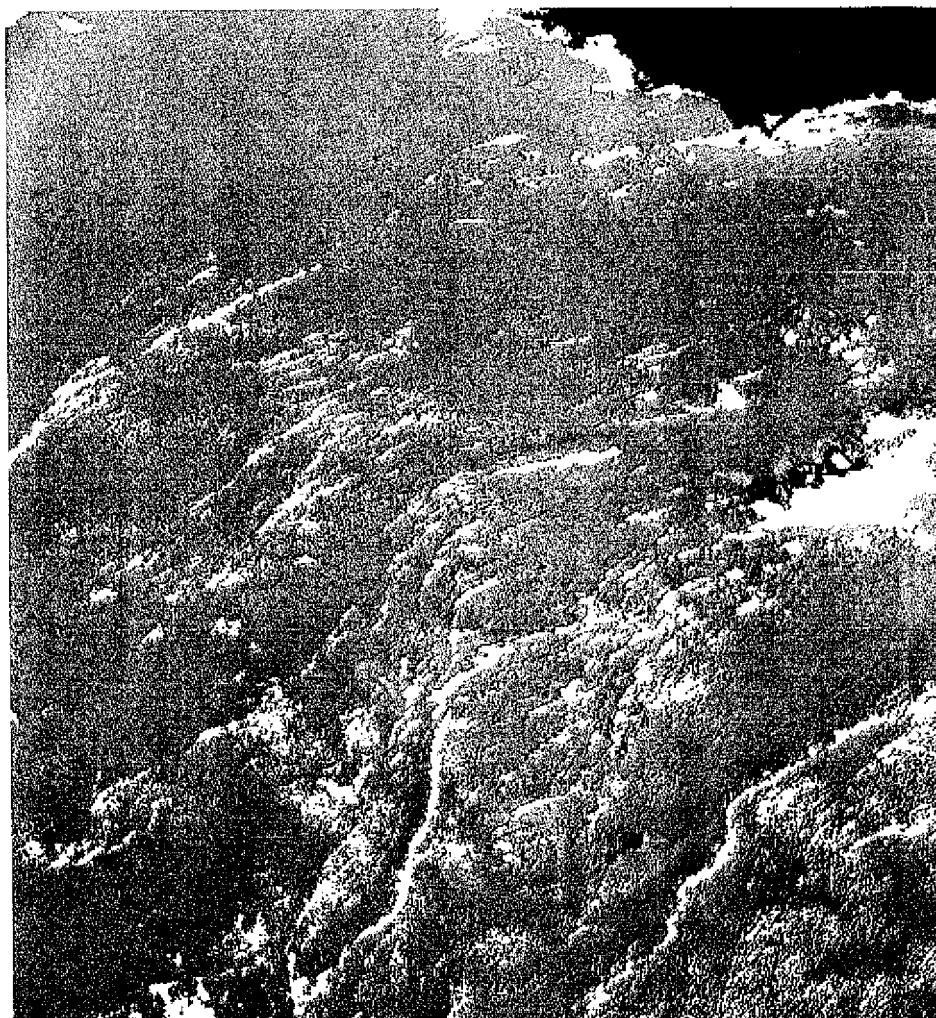
Fig.7. The processed image, with better quality and fewer visible stripes by us-
ing the modified calibration parameters.

concentration computation. By using the modified parameters the processed image is of better
quality and has far fewer visible stripes (Fig. 7).

4.3 Modulation Transfer Function

The square wave modulation transfer function (MTF) requirements for each band at the
Nyquist frequency are specified in Table 5. Each telescope subsystem was carefully designed
to achieve simulated performance with static MTF better than 0.72. With unavoidable align-
ment errors, assembly errors, crosstalks, and simulated satellite motion effects, the instrument
performance nevertheless had good MTF measurement values, between 0.47 and 0.71 (Table

Table 5 . Specification of MTF and pre-launch performance test results.

	Specification		Pre-launch Performance Test Results	
Band No.	Along Track MTF	Cross Track MTF	Along Track MTF	Cross Track MTF
B1	0.21	0.30	0.53	0.68
B2	0.21	0.30	0.55	0.66
B3	0.21	0.30	0.52	0.71
B4	0.20	0.29	0.52	0.58
B5	0.20	0.24	0.53	0.62
B6	0.19	0.16	0.49	0.47
B7	0.20	0.29	0.51	0.68

5). Before launch, the OCI went through dynamic and thermal vacuum tests which caused very little degradation in MTF performance.

Before launch, we measured image sharpness by using a bright object with sharp edges. The measured results, given in Fig. 8, showed good performance that was compatible with the measured MTF. We also performed post-launch measurements by selecting vertical coastlines and measuring the spatial variation of the radiance across the lines (Figs. 9 & 10). The measured results, given in Fig. 11, showed sharpness similar to that of the pre-launch results and suggested that the MTF values should be similar, too.

4.5 Band to Band Spectral Registration

With a 60.7°FOV and 7 focal planes for 7 spectral bands ranging from blue to near infrared, making an opto-mechanical hardware with high accuracy in spectral registration among the bands is a great challenge. To achieve accuracy better than $0.5 \times$ IFOV, tremendous efforts were made in optical design, component fabrication, alignment and assembly to minimize error sources such as mis-alignment and aberration.

The pre-launch test results, given in Fig. 12, showed that the registration distribution was within $\pm 0.36 \times$ IFOV in the along track direction and within $\pm 0.48 \times$ IFOV in the cross track direction. By analyzing in-flight images taken by the OCI we obtained post-launch spectral registration results (Fig. 13) which showed that the distribution was within $\pm 0.40 \times$ IFOV in the along track direction and within $\pm 0.25 \times$ IFOV in the cross track direction.

4.6 Blooming and Sun-Glint Effects

When the OCI is used for observation, some objects such as land and cloud are much brighter than the ocean. Anti-blooming is a CCD feature that can effectively reduce the charge

Image Sharpness Measurement (Pre Launch)
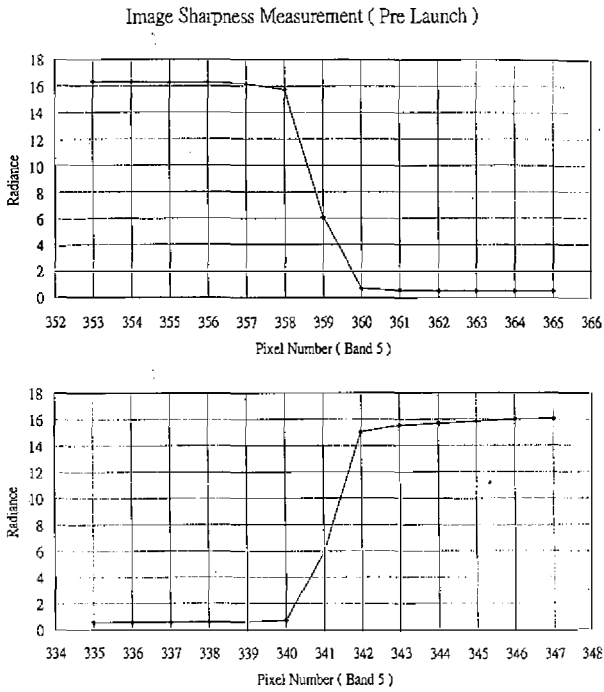
Fig. 8. Before launch, image sharpness was measured by using a bright object with sharp edges. The measured results showed performance that was compatible with MTF.

OCI's Image, $\lambda = 670 \pm 10$ nm.
Date: 03/15/'99
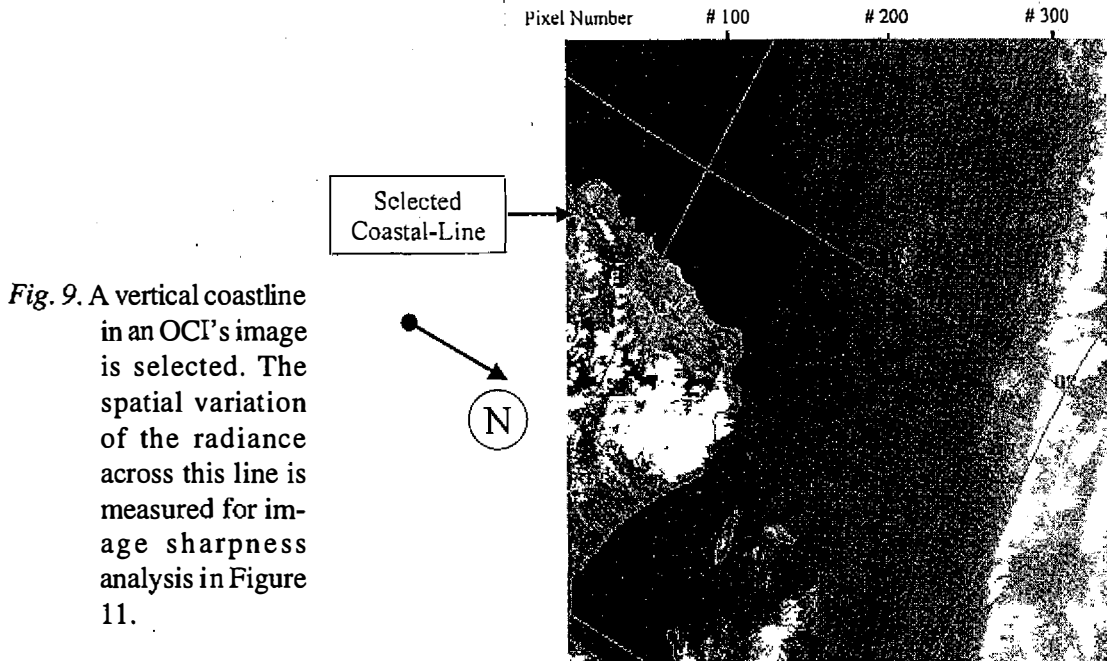
Fig. 9. A vertical coastline in an OCI's image is selected. The spatial variation of the radiance across this line is measured for image sharpness analysis in Figure 11.

OCI's Image, $\lambda = 670 \pm 10$ nm.
Date: 03/19/'99

Pixel Number # 700   # 800   # 896

Fig. 10. A vertical coastline in an OCI's image is selected. The spatial variation of the radiance across this line is measured for image sharpness analysis in Figure 11.

Selected
Coastal-Line

Image Sharpness Measurement (Post Launch)

Pixel Number (Band 5)
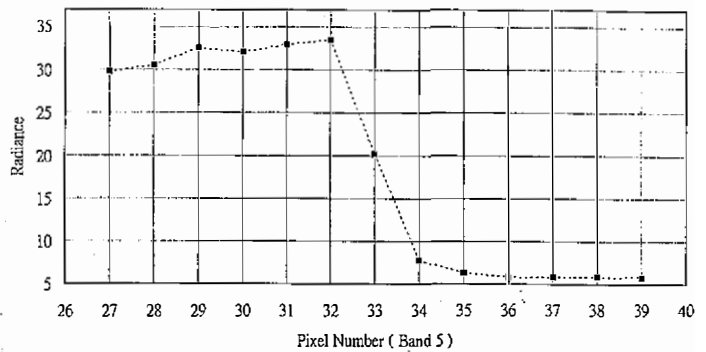
Fig. 11. Image sharpness across the selected coastlines are measured. The results are similar to those of the pre-launch and suggest that the post-launch MTF should be similar to the pre-launch MTF.

Pixel Number (Band 5)

Spectral Registration @ Pixel #895, Pre-Launch
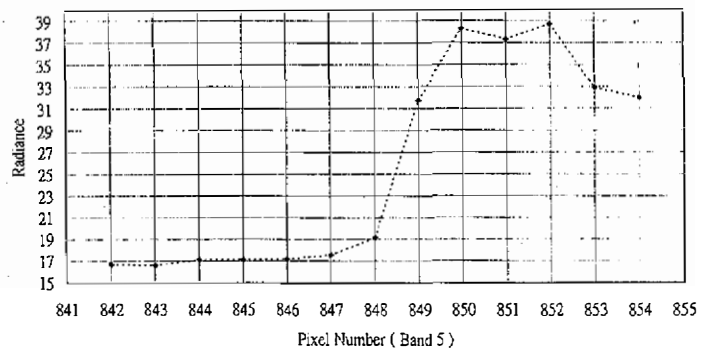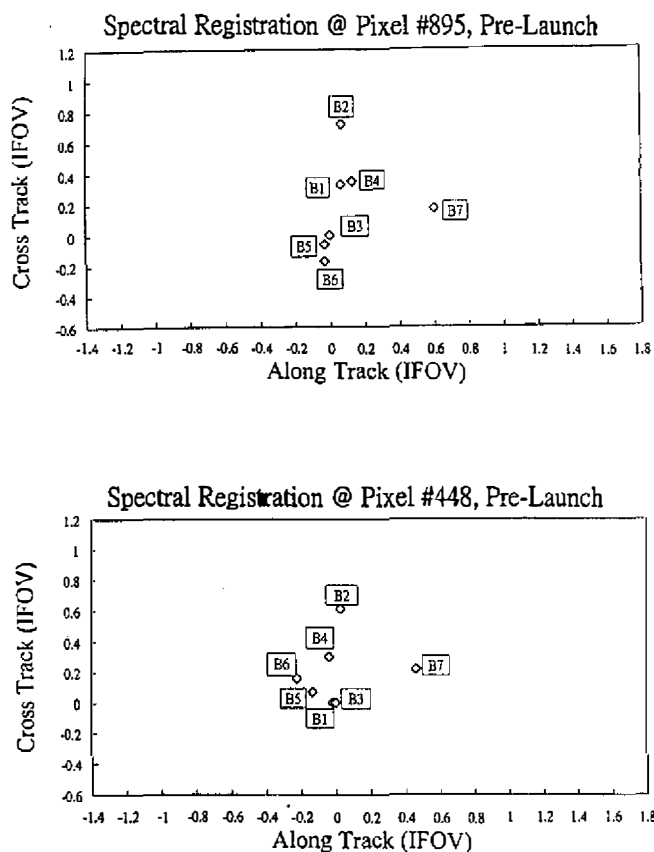
Fig.12. Examples of the pre-launch band to band spectral registration test results. The registration distribution near FOV edge, at pixel #895, is within °"0.31 x IFOV and within ±0.46 × IFOV in the along track direction and cross track direction, respectively. The registration distribution near FOV center, at pixel #448, is within ±0.35 × IFOV and within ±0.32 × IFOV in the along track direction and cross track direction, respectively. The measurement uncertainty is ~ 0.10 IFOV (Instantaneous Field Of View). One IFOV for the OCI is equivalent to 800 meter ground sampling distance.

Spectral Registration @ Pixel #448, Pre-Launch

spill over to the neighborhood when some CCD cells are illuminated by extremely bright incident light. By setting the saturation voltage at 6.5 V on TH7811 CCD chips, a significant anti-blooming feature as well as a very high response linearity over the desired dynamic range were both achieved. The anti-blooming performance for each spectral band was measured by using a bright stripe as the observation object with $20 \times$ IFOV width, and brightness that provided 6 times the saturation radiance. The results showed that blooming effects were limited to only $\leq 5 \times$ IFOVs, or ≤ 10 CCD cells (Fig. 14).

We analyzed the OCI's post-launch imaging data and found that radiance of B6 from land and cloud was 20 and 30 times stronger than the specified mean radiance if image acquisition time was at noon. As a result, even with the anti-blooming feature, the blooming effect could not be easily suppressed for B6 in noontime imagery, especially in the right neighborhood of a large piece of cloud or land. (Fig. 15)

Because the OCI is always viewing in the nadir direction, it is not easy to avoid sun-glint, solar radiance directly reflected from the ocean surface, and its image quality is hence often degraded by this effect if the image acquisition time is around noon, i.e., between 10:30 AM and 1:30 PM local time.(Fig. 16) It is nevertheless possible to significantly reduce this effect provided the imaging schedule is carefully planned. (Fig. 17)

Spectral Registration @ Pixel #895, Post-Launch

Spectral Registration @ Pixel #458, Post-Launch
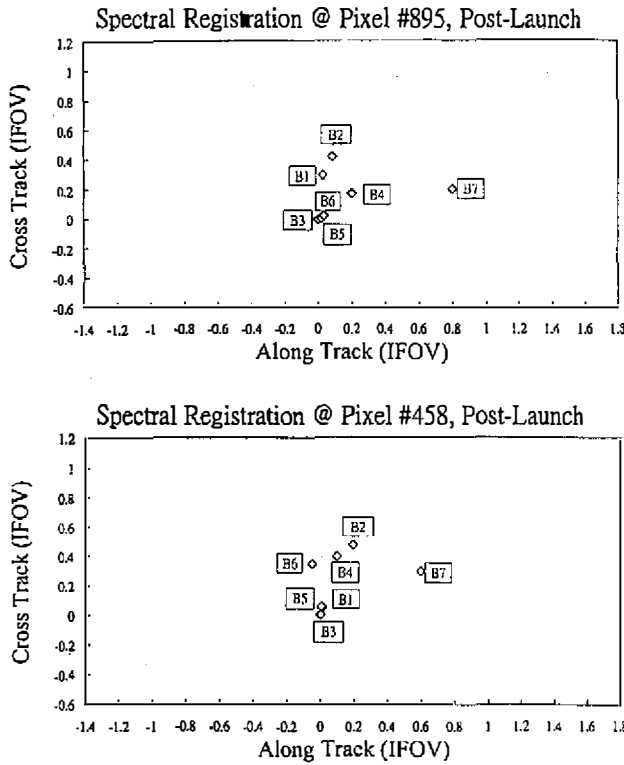
Fig.13. Examples of the post-launch band to band spectral registration test results. The registration distribution near FOV edge, at pixel #895, is within ±0.42 × IFOV and within ±0.22 × IFOV in the along track direction and cross track direction, respectively. The registration distribution near FOV center, at pixel #458, is within ±0.32 × IFOV and within ±0.23 × IFOV in the along track direction and cross track direction, respectively. The measurement uncertainty is ~ 0.15 IFOV.

Fig.14. Two examples of typical anti-blooming measurement results (B3 & B4). A bright strip that generated 1 × the saturation radiance was first used as the observation object for the measurement. The brightness of the strip was later increased to provide 6 × the saturation radiance and the measured results showed that the blooming effect was within 2 pixels on one side and within 5 pixels on the other side.
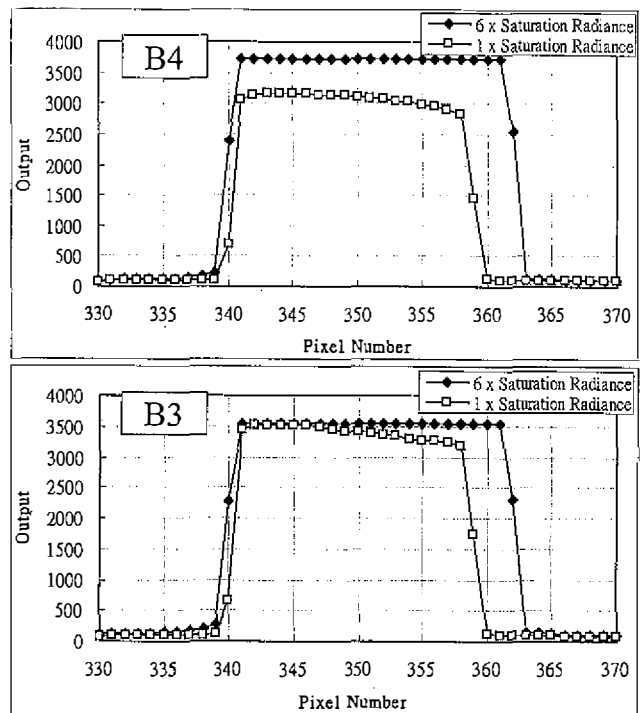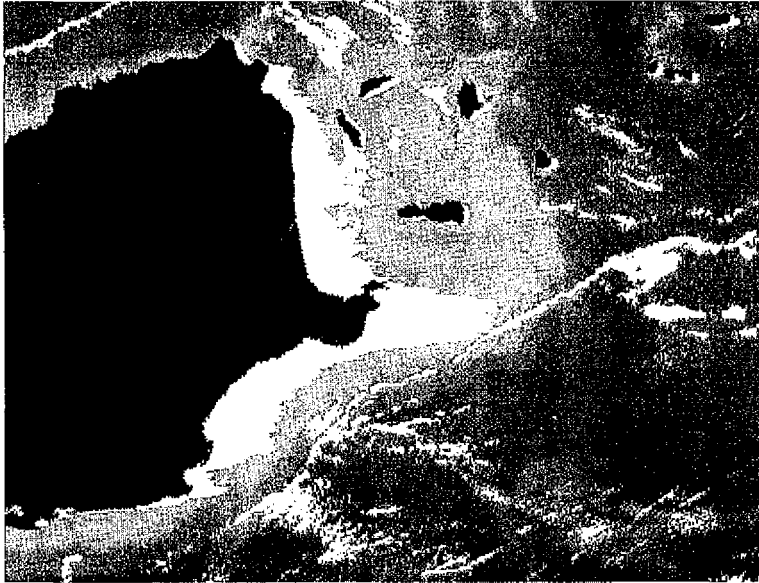
Fig.15. An OCI image acquired near noontime. The blooming effect (white) can still be seen in the neighboring area on the right of a large piece of land (black area).
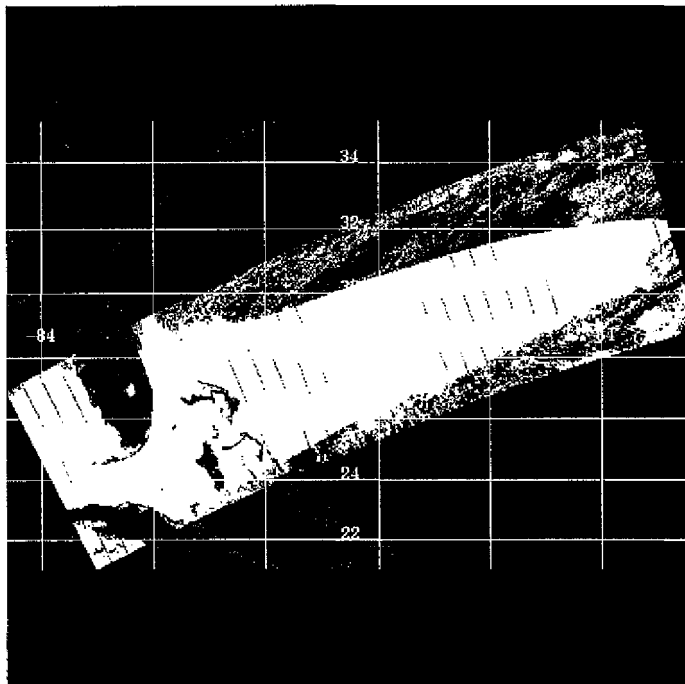
Fig.16. An OCI image with sun-glint effect acquired near noontime.
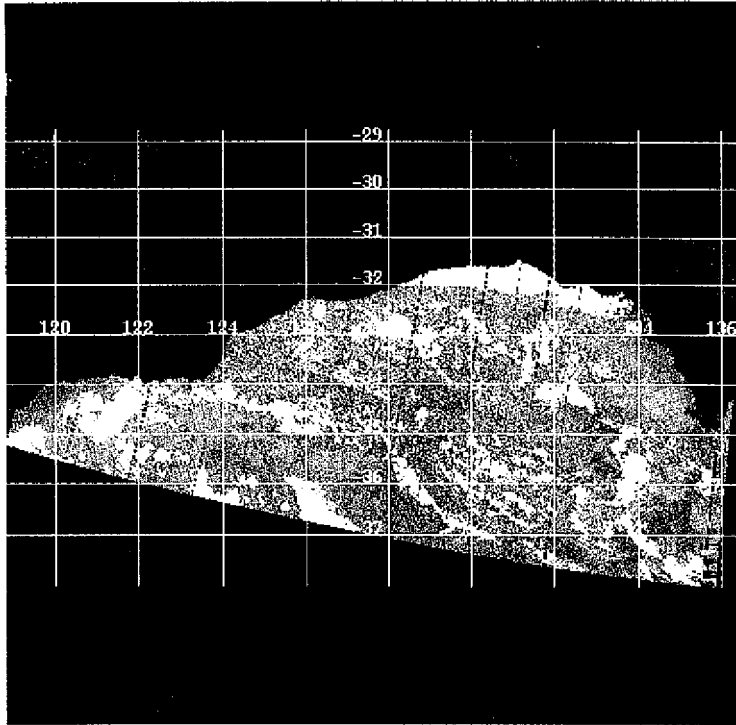
Fig. 17. An OCI image over Great Australian Bight acquired near noontime in
winter. It shows an example of how the sun-glint effect can be avoided if
noontime imaging schedule is carefully planned.

4.7 Dark Signal vs. Temperature

It was found that the OCI's digitized output signals were always greater than zero even
when its total input radiance was zero. The positive values, termed dark signals, were attrib-
uted to offsets and thermal agitation in the CCD cells as well as noise from the CCD cells,
analog electronics and A/D conversion. Dark signals were temperature dependent, and could
vary from band to band as well as from pixel to pixel. We have analyzed many dark signal
data and found that the signal value could be estimated by:

$$\text{Dark Signal (in digital count)} = \text{Circuit Offset} + Rn \bullet 2^{T/Q} \qquad (3)$$

where
"Circuit Offset" = 34.3 ± 2.6, had different values for different CCD chips;
"Rn" = 7.1 ± 1.6, varied from pixel to pixel;
"Q" = $8.9 \pm 1.2°C$, varied from chip to chip; and
"T" was the CCD temperature in °C.

March to August Dark Signal Chart
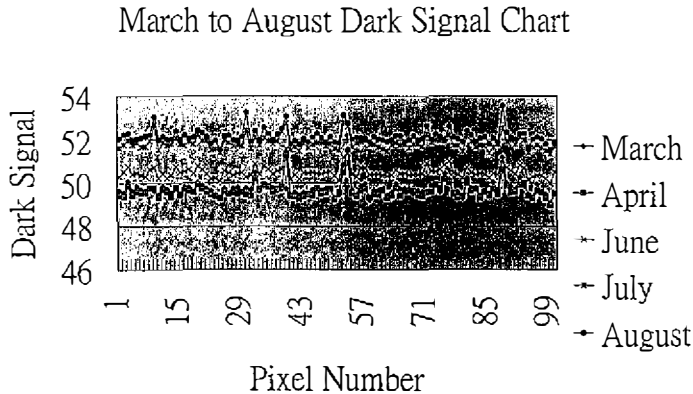
Fig.18. Post-launch dark signal data from early orbit through August 1999. The averaged dark signal value in August 1999 was higher than the early orbit as well as the pre-launch value by ~4 digital counts.

We have also measured post-launch dark signal data and found that the value has increased gradually since April 1999. (Fig. 18) In August 1999, the averaged dark signal value was higher than the pre-launch value by ~4 digital counts. Since the environment of CCD electronics was thermally well controlled to stay within $10\pm2°C$, it was unlikely that the CCD temperature could be as high as 13°C to cause the measured difference of the dark signal. The actual cause is currently regarded as an electronics aging effect, but needs to be investigated in the future. Because the OCI's digitized signal is ~ 1800 with mean input radiance, 4 digital counts is equivalent to 0.22% of the mean signal. It is desirable to take this value into account when we generate the calibration parameters to assure the reliability of data process.

5. CONCLUSION

A spectral radiometer without any moving parts has been built and tested. It is the first space-borne remote sensing instrument with a push-broom scanning mechanism for ocean observation and is a nadir-looking imager with a 60.7° FOV and 800 meter ground resolution at an altitude of 600 km. The results of selected pre-launch and post-launch performance tests have been described. Because of the high performance with reasonable SNR value at relatively weak input radiance, the OCI's observation time could be expanded from 9:00-15:00 to 7:30-16:30 local time at least. To avoid degradation of image quality, noontime imaging should be carefully planned because otherwise the OCI's response could often be saturated by the blooming effect when viewing a large area of land, cloud, or sun-glint region. Since computation of pigment distribution is very sensitive to the uncertainty of radiometric parameters that arises from non-uniformity of radiance from the pre-launch calibration light source, the OCI's image was degraded by non-periodic vertical stripes. We have modified the calibra-

tion parameters and used them to process data and achieve images with improved quality.

REFERENCES

Howard R. Gordon, 1998: In-orbit Calibration Strategy for Ocean Color Sensors. *Remote Sensing and Environment,* **63**, 265-278.

S. B. Hooker, W. E. Esaias, Ci. C. Feldman, W., W. Gregg, and C. R. McClain, 1992: SeaWiFS technical report series volume 1, An Overview of SeaWiFS and Ocean Color. Technical Memorandum 104566, 1, NASA, Greenbelt, MD.

L-S Lee, K. Lo, and Y-J Chiang, 1999: Ocean Color Imager: Instrument Description and its Performance. *TAO, supple. issue*, March, 63-84.

W-S Lin, J-Y Wu, H-J Chiu, C-S Chen, and Y-J Chang, 1999 :Sensor Calibration of the Ocean Color Imager. *TAO, supple. issue*, March, 43-61.

C. R. McClain, W. E. Esaias, W. Barnes, B. Ciuenther, D. Endres, S. B. Hooker, B. G. Mitchell, and. R. Barnes, 1992: SeaWiFS technical report series volume 3, SeaWiFS Calibration and Validation Plan. Technical Memorandum *104566, 3*, NASA, Greenbelt, MD.

Y. Narimatsu, et al., 1997: Ocean Color Imager Instrument: Critical Design Review. NEC Space System Division. OCI-BS-244-NEC.

Y. Narimatsu, et al., 1997: ROCSAT-1 Program: Ocean Color Imager FM Delivery Data Package. NEC Space System Division. OCI-BS-037-NEC.

B. T. Yang, 1995: "The First Ocean Remote Sensing Payload of the ROC: an Introduction." Oceanic Microwave Remote Sensing Workshop.